Sensors and Actuators A 232 (2015) 329–340

Contents lists available at ScienceDirect

Sensors and Actuators A: Physical

journal homepage: www.elsevier.com/locate/sna

Nanostructured graphene–Schottky junction low-bias radiation sensors☆

Mohamed Serry[a,b,*], AbdelHameed Sharaf[b,c], Ahmed Emira[d], Ahmed Abdul-Wahed[b], Asmaa Gamal[b]

[a] Department of Mechanical Engineering, The American University in Cairo (AUC), Egypt
[b] Yousef Jameel Science and Technology Research Center (YJSTRC), The American University in Cairo (AUC), Egypt
[c] Radiation Engineering Department, Egyptian Atomic Energy Authority, Cairo, Egypt
[d] Department of Electrical Engineering, Cairo University, Egypt

ARTICLE INFO

Article history:
Received 31 October 2014
Received in revised form 10 April 2015
Accepted 10 April 2015
Available online 10 June 2015

Keywords:
Radiation sensor
Graphene
Gamma-radiation
Schottky diode
Low-bias
Nanosensor

ABSTRACT

We present a key idea of using the graphene-based Schottky junction to achieve high sensitivity and wide detection range radiation sensors. Nanostructured Schottky junction is formed at the interface between a graphene, metal electrode, and a semiconductor. The current flowing through the junction is mainly controlled by the barrier's height and width. Therefore, the detection principle is based on Schottky barrier height (SBH) modulation in response to different materials and stimuli. We have illustrated the concept for gamma (γ) radiation sensors. It's demonstrated that the integration of graphene leads to a great enhancement in sensitivity of up to 11 times coupled with 5 times increase in the sensing range as compared to conventional Schottky junctions. Furthermore, it was demonstrated that for proposed sensors, that the change in SBH could be fairly linearized as a function in the radiation dose unlike the SBH of comparable conventional junctions. The new concept opens the door for a novel class of minitiuarized, low biased, nanoscale radiation sensors for wireless sensor networks. The devices are based on new nanostructured Schottky junctions made by growing graphene on ultrathin platinum catalytic layer grown on different silicon substrates. Graphene high uniformity film with small flakes size embedded with platinum particles was synthesized using two deposition steps. The integration of graphene layers on regular M–S junctions was only possible by using an ALD grown platinum thin film (10–40 nm) and then growing graphene in PECVD at temperatures lower than platinum silicide formation temperature. The radiation sensing behaviors were investigated using two different substrate types. The first substrate type is a moderately doped *n*-type ($n \approx 2 \times 10^{15}\,\mathrm{cm}^{-3}$) silicon substrate in which a Schottky rectifier response with different threshold voltages was observed. A device that is based on Pt/n-Si conventional Schottky junction was used as a reference. The various devices were exposed to a range of γ-irradiations (2–120 kGy) using Co^{60} source, and a change in terminal voltages before and after radiation were measured accordingly. A sensitivity of 3.259 μA/kGy cm^2 at 1 V bias over a wide detection range has been realized. The charge transport mechanisms are interpreted on the basis of testing the detectors at elevated temperatures and theoretical models, both of which both verified tunneling as the dominant charge transport in the device. Tunneling allowed the operation of the detectors at low bias voltages with good sensitivity. The detector's realized sensitivity at low bias voltage is a significant advantage, allowing the sensor to operate on a small battery or an energy-harvesting source. This is ideal for low-cost wireless sensor networks.

The obtained responses, increase in sensitivity, and increase in detection range, were explained by studying the band diagrams of the graphene–Schottky junction in comparison to that of the conventional junction. Further, the fact that graphene layer was grown on the M–S junction adds to the uniqueness of this research since exfoliated graphene will result in increased contact resistance and lower carrier mobility which might not yield the desired sensing response.

1. Introduction

In the aftermath of the devastating nuclear disaster at the Fukushima reactor facilities in Japan, the development of high-

☆ Selected papers presented at EUROSENSORS 2014, the XXVIII edition of the conference series, Brescia, Italy, September 7–10, 2014.

* Corresponding author at: Department of Mechanical Engineering, The American University in Cairo (AUC), Egypt.
E-mail address: mserry@aucegypt.edu (M. Serry).

http://dx.doi.org/10.1016/j.sna.2015.04.031
0924-4247/

performance ultrasensitive radiation sensor technologies has become paramount. There is a critical need for devices that will actively detect all forms of radiation species (i.e., alpha, beta, gamma, X-ray, and neutrons) and provide continuous monitoring of radioactive material. Moreover, the American National Academy of Engineering has listed the ability to detect nuclear materials at a distance as one of the five major obstacles to preventing nuclear terror [1]. Thus, not only would the implementation of these devices near nuclear facilities be especially advantageous, but it would also be beneficial to install them at national borders to counteract the increased threat of radiological or nuclear terrorist attacks. To accomplish this, the detectors must be small and reliable enough to discriminate among the various types of radiological sources. They would be implemented in portable devices and sensor networks that could be deployed over large geographical areas vulnerable to nuclear radiation or cross-border weapons smuggling.

Detecting small doses of radiation in the environment is critical for communities living close to nuclear plants or in the event of nuclear disasters with International Nuclear Event Scale (INES) of 5 or more, e.g., Fukushima (2011), Chernobyl (1986), and Three Mile Island reactor (1979). With more than 498 power reactors currently operating or under construction in 30 countries [2], accompanied by the unsolved problem of post-process storage of nuclear wastes and reliable controlling of potential environmentally induced leakages, there is an urgent need for relatively cheap and simple to used sensor of a wide range of radiation doses [3,4].

There are three main types of radiation detectors that are commonly used, each having its own method to detect the radiation particles. They are divided into gas-based detectors [5–9] which use a gas that is electrically biased to collect ionized particles, which are a result of the interaction between the radiation particle and the fill gas, semiconductor detectors [10–14] which rely on a reverse biased diode junction to create electron hole pairs when the depletion region is excited by incoming radiation particles, and scintillator detectors [15–22] which interact with incoming radiation particles and, as a result, release light photons that are detected using an optical transducer. Nanostructured materials on MEMS integrated devices could replace most current conventional radiation sensors, the majority of which rely mainly on lattice defects in single crystal silicon structures that are induced by irradiation [23]. These defects are detected through resistance or capacitance changes. The current MEMS based radiation techniques, however, have substantial drawbacks: (1) limited sensitivity. (2) Limited detection range (efficient at high doses of 60 kGy or higher). (3) Limited efficacy (one time use), and (4) High probability of error.Increasing surface to volume ratio and increasing material's selectivity could potentially overcome the limited detection range and low sensitivity of conventional MEMS based capacitive radiation sensors.

P-n structured diodes and Schottky diode-based radiation sensors are gaining much attention since the 1990s, in particular for biomedical and imaging applications [24,25]. However, they normally operate at high reverse voltage (500–1500 V) such that the space charge region is wide enough to increase the generation/recombination currents.Therefore, the problem of leakage current should be overcome [26].

Integration of nanomaterials with solid-state radiation sensors is undertaken in order to enhance sensitivity and improve device efficiency and capacity [27–31]. More importantly the devices can operate at low bias and therefore increase the possibility of operating these detectors on small batteries or energy harvesting sources, which is not possible with the current state-of-the-art detectors. However, along with the ability to scale down devices come challenges with designing and developing nanostructures that must operate properly in an increasingly smaller environment. Schottky diode can replace conventional PN junctions and bipolar transistors in the scaled down solid-state sensors due to their fast response and low threshold voltages. Schottky diode based sensor generally consists of a metal-semiconductor (M–S) junction. The most common choices of metals are catalytic type noble metals (e.g., Au, Pt, and Pd) [32–35]. Schottky diodes have been implemented for developing highly efficient sensors, solar cells and electrochromic devices [36–40]. Graphene ultrathin sheets are emerging as ideal candidates for thin-film devices and combination with other semiconductor materials such as silicon. They have been produced in the form of ultrathin sheets consisting of one or a few atomic layers directly grown by chemical vapor deposition (CVD) [41–43] or by solution processing [42,45] and then transferred to various substrates.

In this paper we havee implemented a direct, simple, reusable, isotropic, wide range, and ultrahigh sensitive radiation sensor. The sensor is based on a nanostructured array of graphene grown on platinum/n-Si substrate. The new sensor structure (Fig. 1) is a Schottky barrier diode based on forming an M–S junction of *n*-type silicon substrate and ultrathin film platinum integrated with graphene layer. The high carrier mobility in graphene and the ultrathin platinum film facilitate generating a strong forward current in response to γ-irradiations. The results show that this new structure gives a signal that is an order of magnitude higher than a conventional Schottky barrier diode exposed to the same radiation doses.

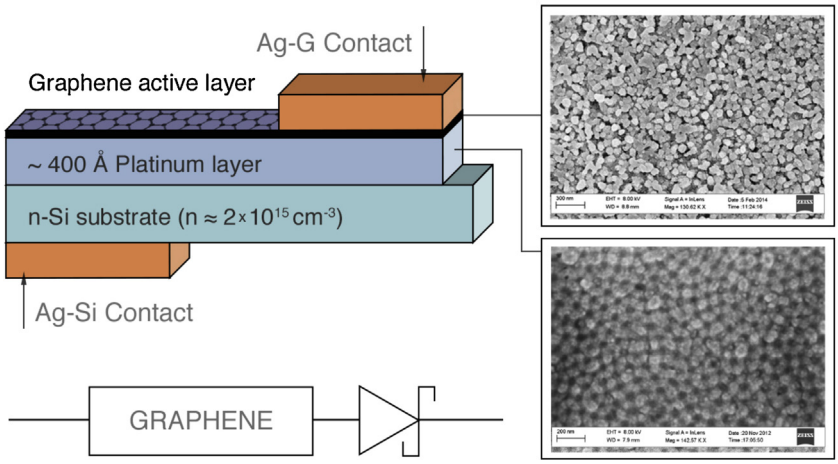

Fig. 1. Schematic diagram of the working principle of the graphene based Schottky junction sensor showing SEM images of the top view of the graphene and platinum thin films.

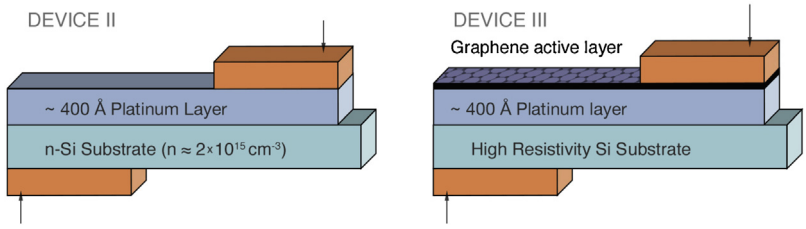

Fig. 2. Schematic of the two types of devices fabricated for comparison (a) the conventional Schottky device; (b) the high resistivity Si substrate device.

Further, more structures based on different substrate doping levels were fabricated and analyzed (Fig. 2). The studied devices show a promise for high sensitivity, low power, and wide detection range. Different current flow regimes were investigated in order to tune the sensor structure/parameters is presented accordingly. Consequently, the proposed low-biased graphene based nanostructured devices enabled the realization of a new set of radiation sensing devices with high sensitivity, fast response time, and the possibility of operating on low power source (e.g., operating on 1.5 V coin battery), which is significant for implementation in wireless sensor arrays by integrating them on SAW platforms to sense the change in current wireless [46–48]. Finally, the proposed sensing principle can be efficiently implemented for various types of radiation species (i.e., alpha, beta, gamma, X-ray, and neutrons).

Finally, The proposed sensors operate on low bias voltage, are isotropic (i.e., independent of the radiation exposure angle), easy to fabricate, can operate wirelessly, and can be seamlessly integrated in wearable detection devices for ultrahigh sensitivity online monitoring of γ-ray irradiations.

2. Experimental procedures

2.1. Fabrication

Graphene high uniformity film with small flakes size embedded with platinum particles was synthesized using two deposition steps. The first deposition step of the platinum catalysis was performed in Atomic Layer Deposition (ALD) using Cambridge NanoTech Savannah ALD deposition system. The precursor used was Trimethyl(methylcyclopentadienyl) platinum(IV) with high purity O_2 used as an oxidizing agent. Deposition temperature is 275 °C for 50–300 cycles to produce the catalysis Pt thin film in thickness around 40–300 Å. The second deposition step was utilized Plasma Enhance Chemical Vapor deposition (PECVD) using Oxford Instruments, PlasmaLab 100 PECVD System at 600 °C. The pressure is maintained at 1500 mTorr and the chamber is heated up to 600 °C in methane (CH_4) rich environment.

2.2. Structural characterization

X-ray photo-electron spectroscopy (XPS) characterization data were performed on K-AlphaXPS from Thermo Scientific in the range of 1–1350 eV to inspect the surface chemistry of the graphene. Raman spectra of the graphene thin film were obtained by Enwave Optoronics Raman Spectroscope (λ_{ex} = 532 nm, P = 500 mW, acquisition time = 10 s). Atomic force microscopy (AFM) from Bruker, and field emission scanning electron microscopy (FE-SEM) from Zeisswere used for structural and morphological characterizations.

2.3. Measurement procedure

All the fabricated samples were subsequently irradiated with γ-photons from cobalt 60 (Co^{60}) source; the irradiation dosages are adjusted through the exposure times at an approximate rate of 25 min per 1 kGy. Example radiation doses for different samples are listed in Table 1. The samples were connected according to the circuit show in Fig. 3 and the I–V characteristics for different samples were measured using the 4156C high precision semiconductor parameter analyzer before and after irradiation. All samples are irradiated with 2–5 kGy dose, then measuring the I–V characteristic and re-irradiated with another 5 kGy dose. This process is repeated several times up to cumulative dose of 120 kGy. I–V measurements

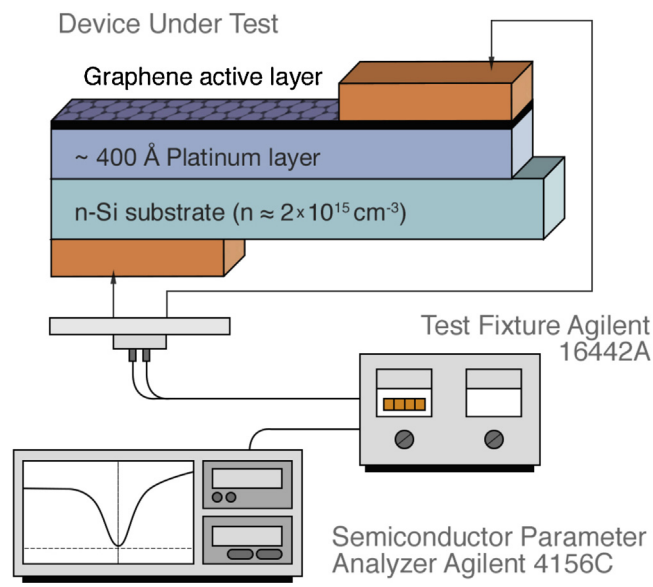

Fig. 3. Schematic of the measurement setup used to obtain the I–V characteristics of the different devices.

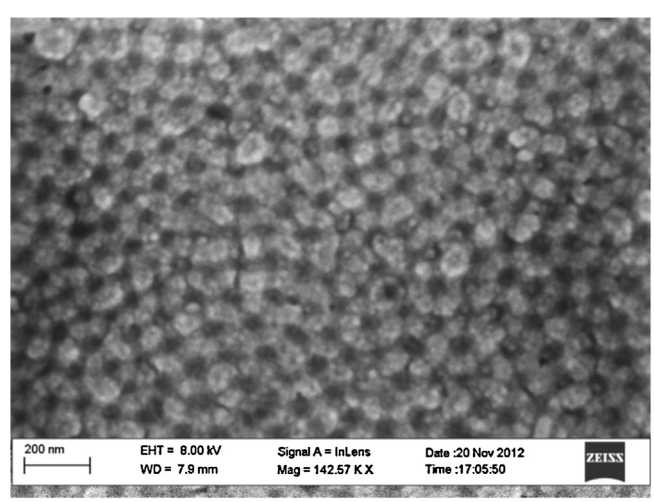

Fig. 4. Top view SEM of platinum thin film deposited by ALD for 150 cycles at 275 °C, indicating the nanoparticle Pt structure.

Table 1
An example of radiation doses for different samples.

Device #	Device configurations	Initial radiation doses (kGy)	Subsequent repeated adiation doses (kGy)	Total cumulative doses (kGy)
Device 1	G/Pt/n-Si	2 and 5	5	120
Device 2	Pt/n-Si	2 and 5	5	120
Device 3	Pt/Hi--resistivity Si Si	5	5	60
Device 4	Pt/SiN/n-Si	10	5	60

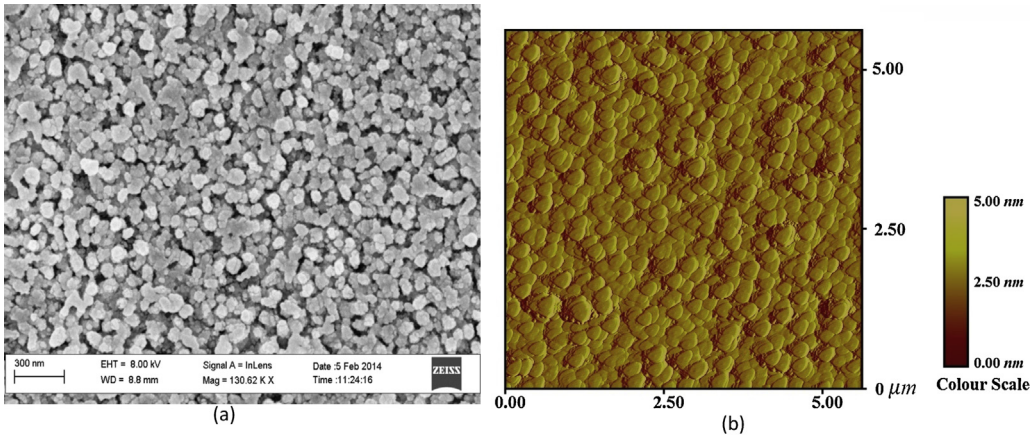

Fig. 5. (a) Top view SEM image of the graphene thin film, and (b) top view AFM image of $5 \times 5\ \mu m^2$ area of the graphene layer showing maximum height of 5 nm.

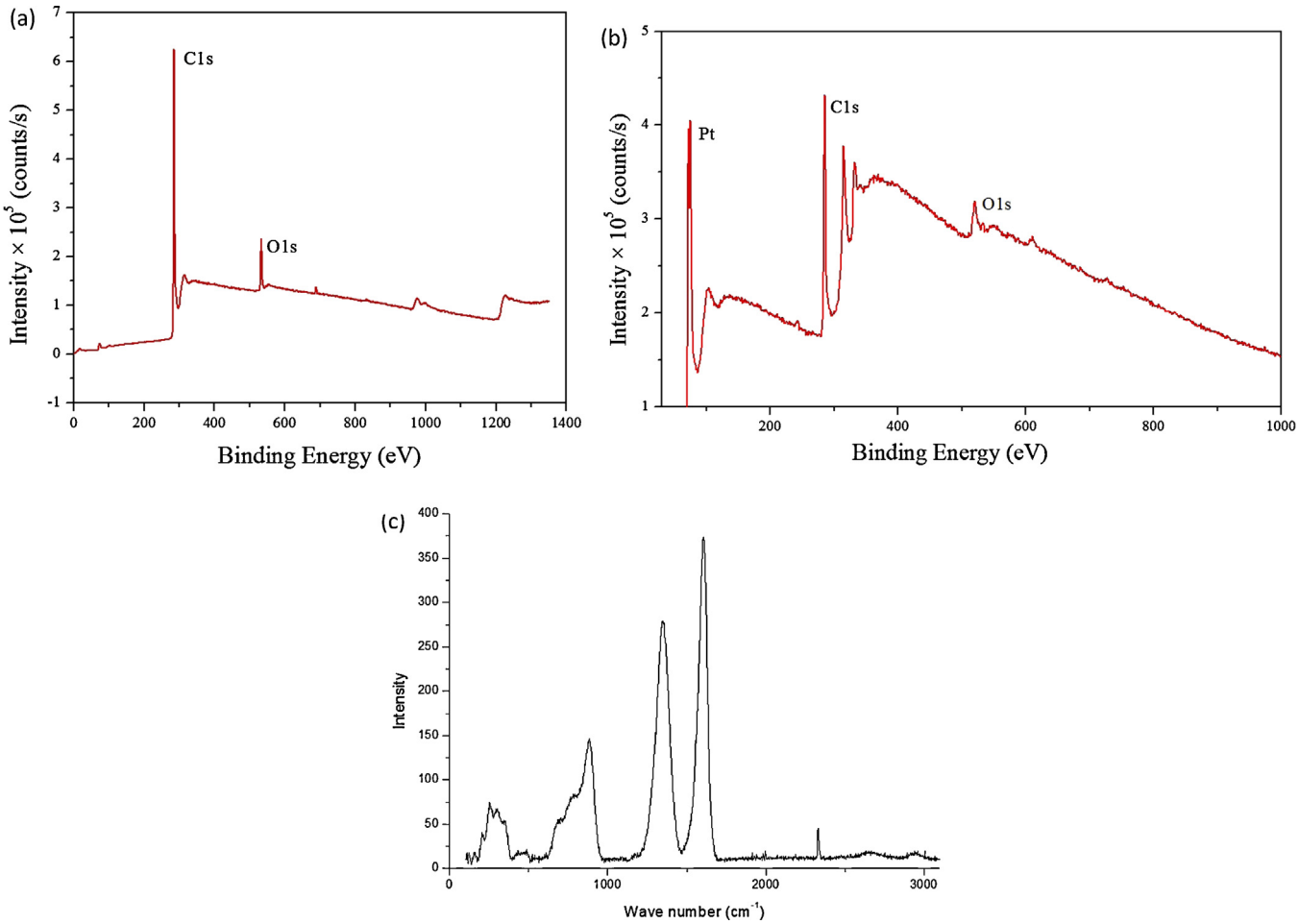

Fig. 6. (a) XPS survey spectra on the surface of the graphene film indicating carbon peak and oxygen contamination; (b) Deep XPS survey after 10 s etching the surface indicating the carbon and platinum peaks, and no oxygen peaks; and (c) Raman spectrum of the graphene thin film indicating the D, G and D + D" peaks. The shift in the G is due to the doping with platinum.

were also conducted at elevated temperatures (40–160 °C) in order to verify the dominating carrier transport mechanisms.

3. Results and discussion

3.1. Morphology and structural properties

The SEM images of the top view of Pt catalysis layer after ALD deposition is presented in Fig. 4. The thickness of the film in this figure is ~120 Å. From Fig. 4 it is observed that Pt film is made of fairly organized hexagonal close-packed particles with diameters ranging from 30 to 40 nm. Fig. 5(a) shows the top view image of the graphene film. It is observed from the figure that the film is made of highly packed columnar nanostructured network that is close to the structure of the underlying Pt catalysis layer. Fig 5(b) shows the AFM image of the graphene layer with maximum height of 5 nm above the surface. The XPS analysis was carried out in order to investigate the elemental composition of the film. As depicted in Fig. 6(a) XPS survey spectra of the graphene surface shows the presence of C, with very little O_2 as a contaminant. This is evident by the C1s peak at binding energy of 285.11 eV and the O1s at binding energy of 533 eV. It is observed that the peaks obtained were in agreement with previous reports, indicating that the film consists of graphene. Fig. 6(b) depicts the XPS survey after etching the surface for 10 s. The peaks in this figure can be resolved into three main peaks with binding energies of 75.08 eV for Pt, 285.08 eV for C, and 520.08 eV for O_2 contaminants, respectively. The presence of Pt within the layer is the main source of *p*-doping of the graphene layer. Fig 6(c) shows the Raman spectrum of the graphene surface. The figure displays the graphene's D, G, D + D" bands, and a slightly flat 2D band. The shift in the G band can be attributed to the doping of the graphene with the platinum layer [44,45].

3.2. Sensing mechanism: G/Pt/n-Si junction

The working principle of our new device design is based on the interaction of γ-photons with the graphene layer which changes the local electric field distribution and thus thevariation of the Schottky barrier height (SBH) at the Pt/n-Si junction, resulting in a detectable current change, we refer to it as graphene–metal–semiconductor junction. As schematically shown in Fig. 7, when graphene is positively biased and in contact with Pt it becomes *p*-doped and its Fermi level (E_f) is lowered. Therefore, as γ-photons penetrate through the bulk of the whole device, there are no graphene electrons available for interband transition especially at lower radiation doses (Fig. 7(a)).

Meanwhile, at the Pt/n-Si interface, when a forward-bias voltage is applied to the device depicted in Fig. 7, the work function of Pt (~5.7–5.98 eV) is greater than that of the n-Si (4.5 eV), therefore the contact potential is reduced. Thus, the electrons move from the conduction band across the depletion region to the metal, creating a forward current (I_{fwd}) through the junction. The current across a Pt/n-Si junction is mainly due to majority carriers, unlike pn junctions where current is mainly carried by minority carriers. Moreover, there are three main mechanisms by which current can flow: (1) diffusion of carriers, (2) thermionic emission, (3) quantum mechanical tunneling. Both diffusion and thermionic emission mechanisms result in rectifying exponential I–V characteristics, and they dominate in moderately doped semiconductors. According to the thermionic emission and diffusion theories of Schottky diodes, the dependence of forward current on the applied voltage is given by the expression [49]:

$$I = I_s \left\{ \exp\left(\frac{qV}{kT}\right) - 1 \right\} \quad (1)$$

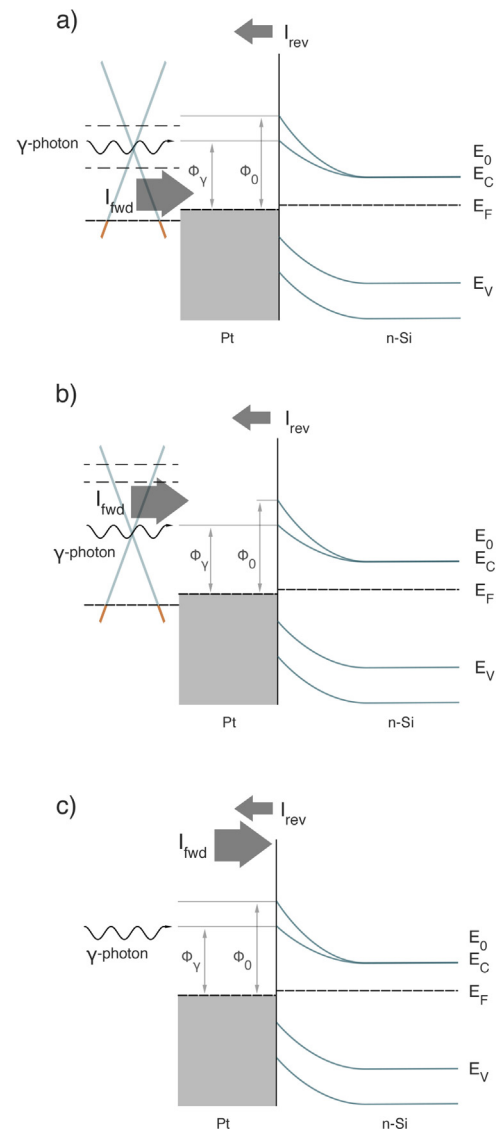

Fig. 7. The energy-band diagram at interface of graphene/Pt/n-Si junction where a Schottky barrier is formed. (a) The graphene–Schottky device at lower doses, when graphene is positively charged, the Fermi level (Ef) is lowered. Upon gamma irradiation, e–h pair is formed in Si lowering the SBH, while in graphene there is no electron available for the interband transition, a strong forward current will flow from Si to graphene. (b) at higher doses graphene electrons are excited to higher states increasing the reverse current and therefore reduce the overall net current, (c) for the conventional Pt/n-Si Schottky junction, forward current is induced at lower doses but the response is saturated at higher doses due to the counterbalancing induced reverse current.

where q is the charge of one electron, V the applied voltage, T the absolute temperature in kelvin, k is the Bolstmann's contstant, and is is the saturation current as defined by:

$$I_s = AA^{**}T^2 \exp\left(-\frac{q\phi}{kT}\right) \quad (2)$$

in which A is the junction's surface area, A^{**} the Richardson constant and ϕ is the zero bias Schottky barrier hight in eV. On the other hand, the more dominant tunneling mechanism in heavily doped semiconductor. Si–Pt interface lattice defects also gives rise to carrier tunneling across the Schottky barrier [46]. Tunneling results in a leaky Schottky diode with symmetrical I–V characteristics.

Measurements of the dark current versus applied voltage is shown in Fig. 8 where the I–V characterisitc is nearly symmetrical. The semilog I–V (ln(I) versus V) characteristic is also plotted in

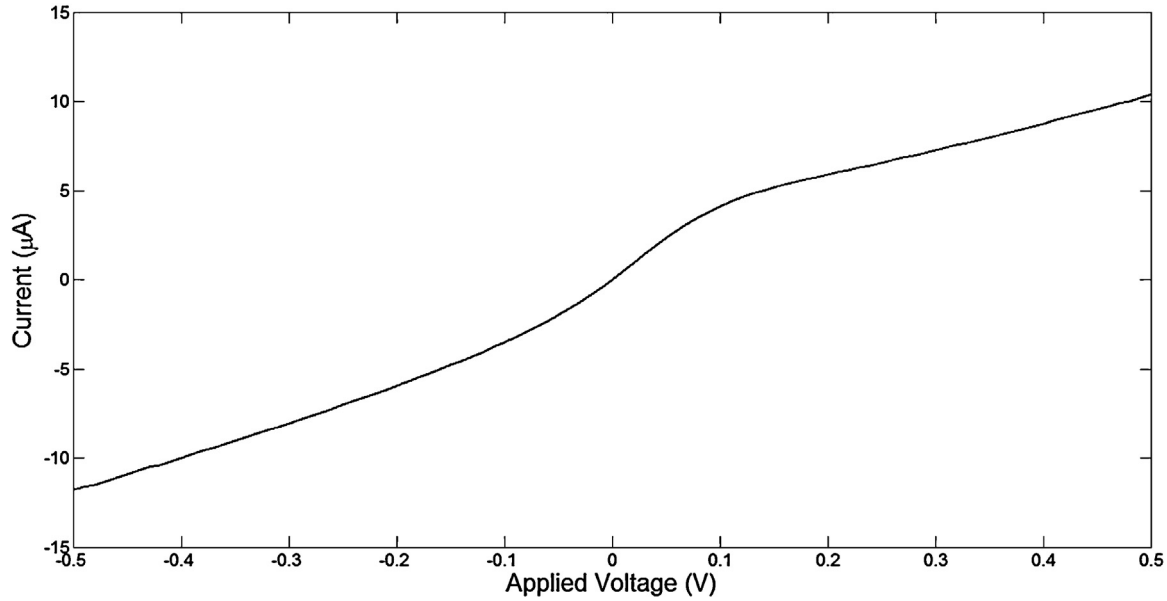

Fig. 8. Dark I–V curve in absence of radiation.

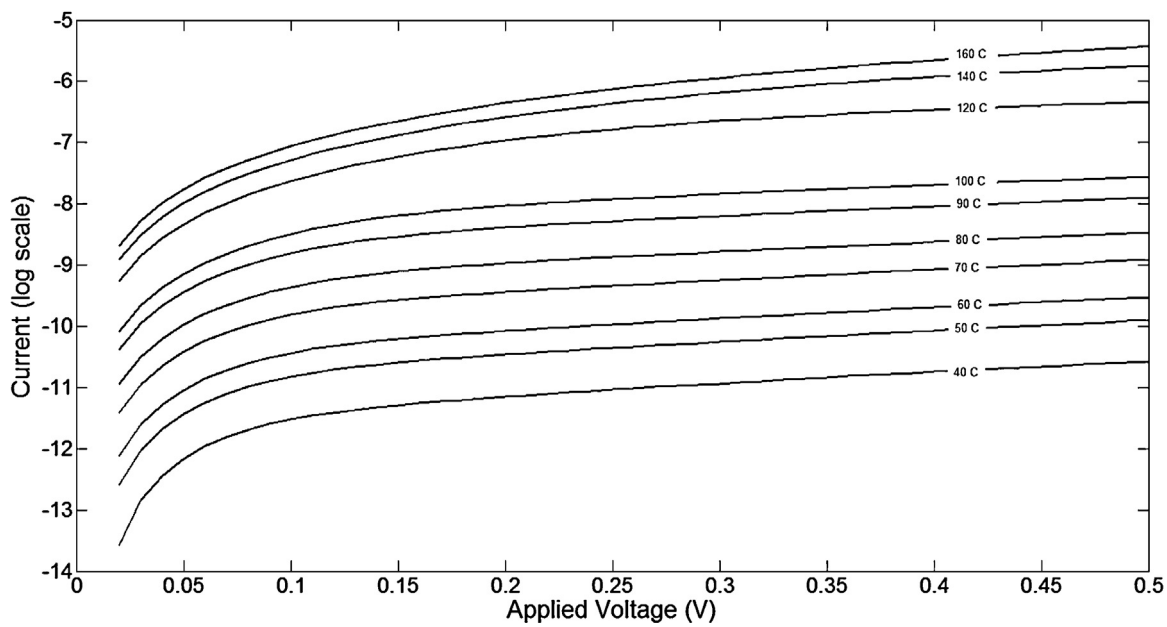

Fig. 9. I–V characteristics of 4 kGy irradiated graphene–Schottky junction at different temperatures.

Fig. 9 at different temperatures from 40 °C to 160 °C. It is observed that the slopes in the semilog scale is independent of temperature, which is commonly observed in Schottky diodes dominated by tunneling current [50–53]. This is in contrast to the thermionic emission model predicted by Eq. (1), where the slope of ln(I)–V characteristics is inversely proportional to absolute temperature T. As the Pt/n-Si junction is exposed to γ-photons, more bonds are broken in the Si lattice, which results in the freeing of more electrons and shifts the Fermi level up. When the fermi level shifts up, the barrier height decreases, which results in an increase of the tunneling current according to the following equation [54]:

$$I = Aqv_{R^n}\exp\left(-\frac{4}{3}\frac{\sqrt{2qm*}}{h}\frac{\phi^{3/2}}{\epsilon}\right) \quad (3)$$

where $v_R = \sqrt{\frac{KT}{2\pi m}}$ and $\epsilon = \frac{\phi_B}{W}$.

In the above equation, q is the charge of electrons, v_R is Richardson velocity, n is the density of carriers in the semiconductor, m^* is the effective mass of electrons in n-silicon, ϕ is the barrier height, ϵ is the electric field and w is the barrier width. It is clear from the tunneling current equation that if the barrier height is modulated (by gamma irradiation), a change in the current is observed. Consequently, the change in SBH can be obtained by diffrentiating (3):

$$\Delta\phi_B = -\frac{3}{2}\frac{h}{Aqv_{R^n}\sqrt{2qm*w}}\sqrt{\phi}\exp\left(\frac{4}{3}\frac{\sqrt{2qm*}}{h}w\sqrt{\phi}\right)\Delta I \quad (4)$$

The relationship between radiaton dose and barrier height is linear at low doses (as discussed in Section 3.5, and shown in Fig 12(a)), therefore the change in barrier height for a given dose can be cal-

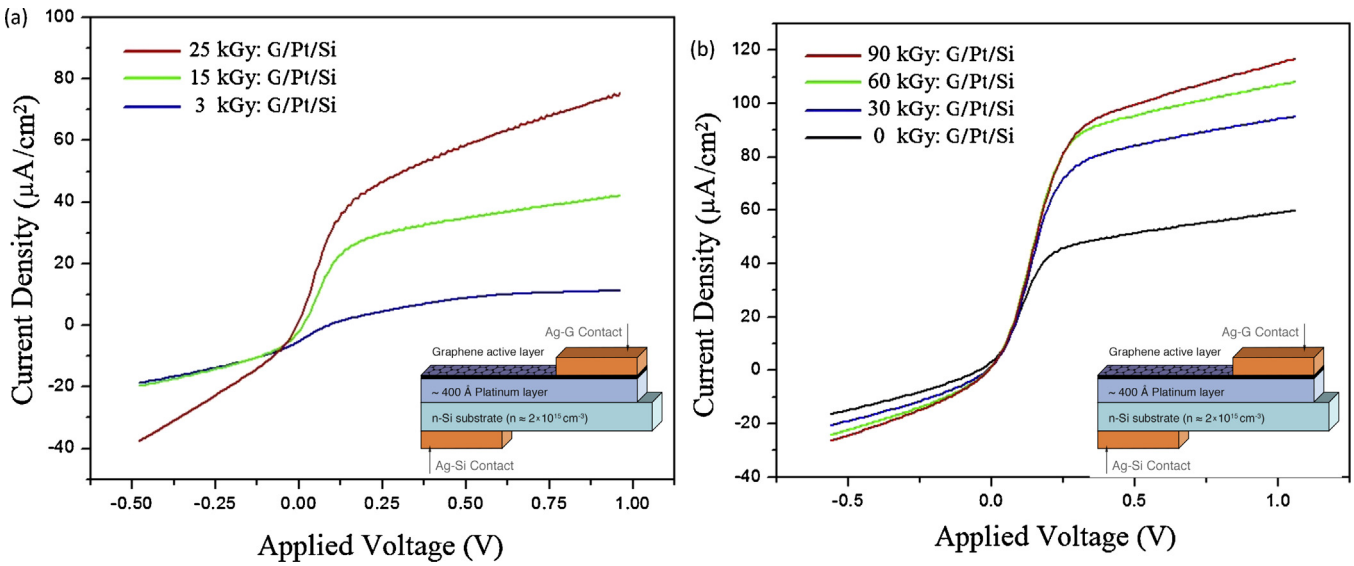

Fig. 10. I–V characteristics of graphene–Schottky device at room temperature in response to (a) low radiation doses; (b) high radiation doses.

culated from the Eq. (5), and the resulting barrier height due to gamma irradiation is:

$$\phi_\gamma = \phi_{B_o} + \Delta\phi_B \tag{5}$$

where ϕ_{B_o} is SBH before exposure to γ-irradiation.

Therefore, in the case of forward voltage bias, the intimate junction with the *p*-doped graphene layer coupled with interaction with γ-photons result in shifting the SBH down as expressed in Eq. (5). As a result, a reverse current (I_{rev}) is induced in the Si–G direction. Meanwhile, the released electrons reduce the thickness of the depletion region resulting in forward current (I_{fwd}) induced in the G–Si direction (Fig. 7(a) and (b)). The net current flow can be determined according to:

$$I_{net} = I_{fwd} - I_{rev}. \tag{6}$$

At low radiation doses, the forward current is much larger than the reverse current because half of the photon energy excites most graphene electrons to states lower than the Si conduction band (E_c). However, at higher radiation doses, half the photon energy excites electrons to higher levels which leads to reducing the SBH. Therefore a stronger reverse current is generated which lowers the device sensitivity.

The sensing behavior at low and high radiation doses can be summarized with the aid of Fig. 7(a) and (b) as follows: graphene layer is *p*-doped as contact is established with Pt, in addition to further lowering of the graphene's Fermi level due to positive biasing. Both effects, result in further lowering of the SBH of the junction which results in a stronger forward current as compared to the conventional junction. In response to γ-irradiations, SBH is reduced further resulting in a stronger forward current, whereas at the graphene interface, the half γ-photon energy is insufficient to excite the graphene electrons for interband transition which results in a weak reverse current. This phenomenon is also responsible for the increase in the detection range of the graphene-based devices as compared to the conventional ones due to the increase in the vacant states for the source electrons, which get saturated faster in conventional junctions under very high radiation doses (Fig. 7(c)).

3.3. γ-Irradiations sensing behaviors

Fig. 10 shows the I–V characteristics of the graphene–Schottky device at room temperature after exposure to low (Fig. 10(a)) and high (Fig. 10(b)) radiation doses, respectively. In order to

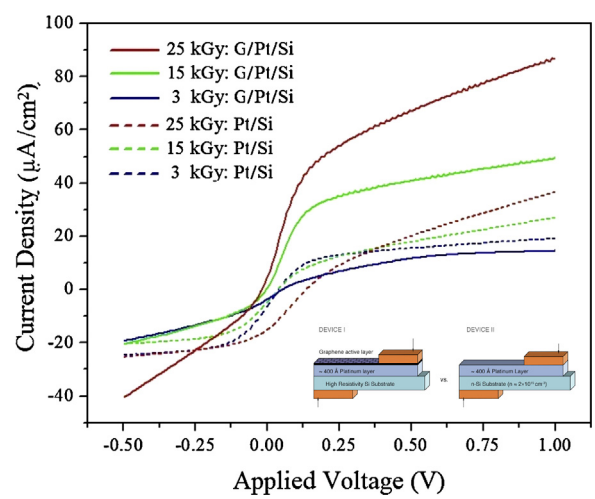

Fig. 11. Comparison of the I–V characteristics of the proposed graphene–Schottky vs. a conventional Schottky junction in response to different radiation doses clearly indicating higher output current for the proposed device.

exhibit the role of the proposed structure more clearly devices with a convetinoal contact were also irradiated simulateneously for comparison, these devices are referred to as Pt/n-Si devices. Comparison between the I–V curves at room temperature for the graphene–Schottky and Pt/n-Si devices at different radiation doses are demonstrated in Fig. 11. From the figure, it is observed that the sensors with conventional Pt/n-Si contact gives the lowest forward current value at all votages in comparison to graphene–Schottky contact. This is owening to the high Schottky barrier height (SBH) for Pt/n-Si device and stresses the fact that the current is mainly governed by the SBH. Fig. 10 clearly illustrates the advantage of our proposed device as up to an order of magnitude increase in the output current could be obtained as compared to the conventional Pt/n-Si junction.

3.4. Detection range and sensitivity

Fig. 12 shows the output current versus irradiation dose at different bias voltages for graphene–Schottky (Fig. 12(a)), and Pt/n-Si (Fig. 12(b)) devices, respectively. The curves in Fig. 12(a) clearly indicate higher response at lower doses while the curves flatten at

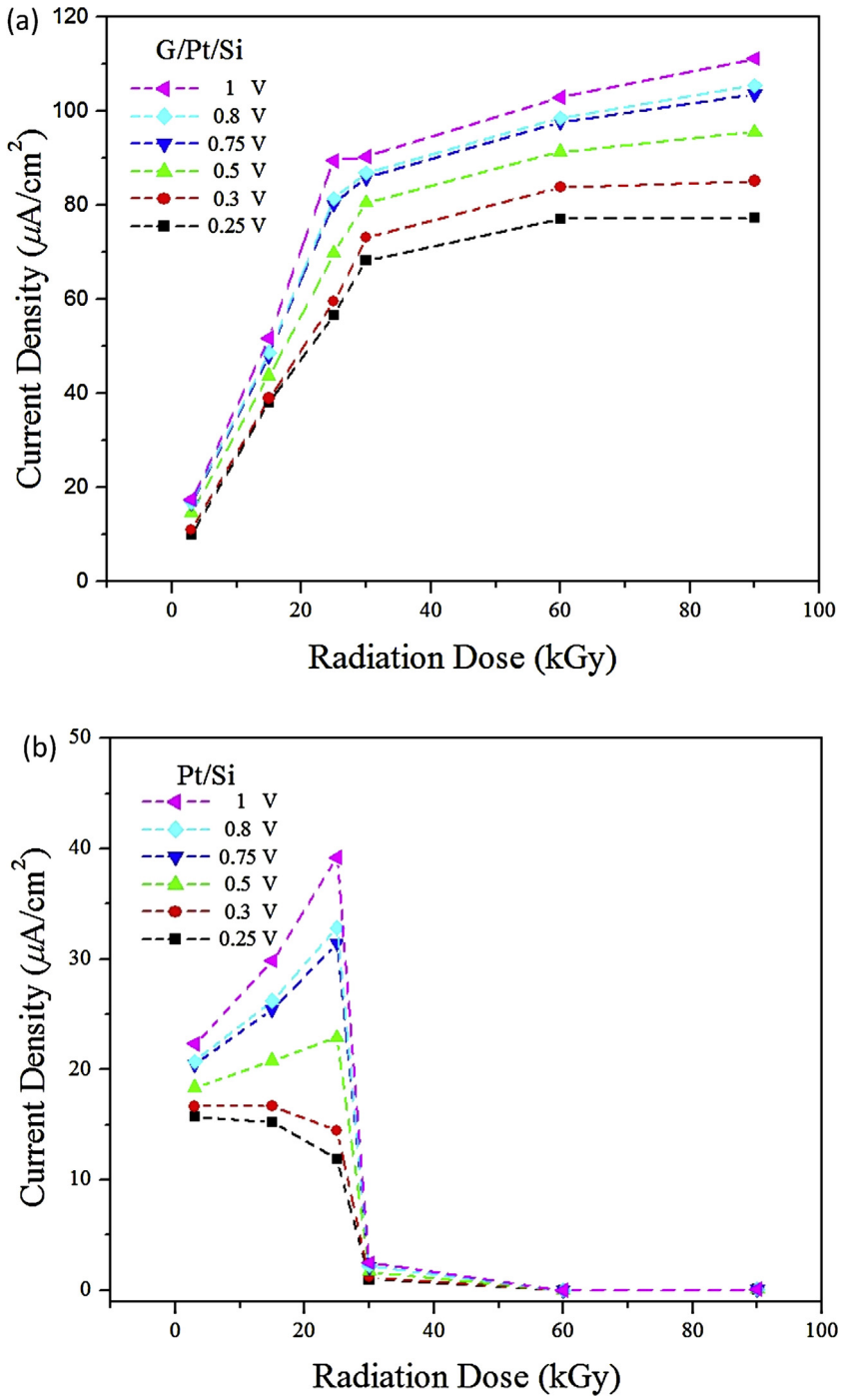

Fig. 12. Effect of radiation dose on current density at different bias voltages for (a) graphene–Schottky devices indicating high sensitivity at higher doses; and (b) conventional Pt/n-Si Schottky junction, indicating insensitive response at higher radiation doses.

higher doses due to the increased reverse current as discussed in the previous section. Whereas, for the conventional Pt/n-Si devices a significant drop in the current is observed at higher doses which can be attributed to the saturation of the forward current as explained earlier.

Fig. 13(a)–(d) demonstrate the sensitivity of the graphene–Schottcky device at low and high doses. Fig. 13(a) and (b) show that a sensitivity of up to 3.259 μA/kGy cm^2 at 1 V bias can be realized at low irradiation doses, while the devices are not comparably sensitive at higher doses. As shown in Fig. 13(c) and (d), a drop in sensitivity to 0.3463 μA/kGy cm^2 at 1 V bias is observed at higher radiation doses. Fig. 14 demonstrates that sensitivity of the device can be linearized with respect to the applied voltage at both higher and lower doses, which is inline with the linearization in SBH that was noted earlier. A comparison between the responses of different sensors biased at 0.25, 0.5, 0.75, and 1 V after being exposed to low and high radiation doses is shown in Fig 15(a)–(d). The figures clearly demonstrate the higher sensitivity of the graphene–Schottky device as compared to the conventional Pt/n-Si junction of the same size and bias voltage. Fig. 15 also clearly shows that the conventional junction devices become almost insensitive to higher radiation doses whereas the proposed devices clearly exhibit higher detection ranges from 2 to 120 kGy (Fig. 15). Finally, Fig. 16 demonstrates that up to 11 times

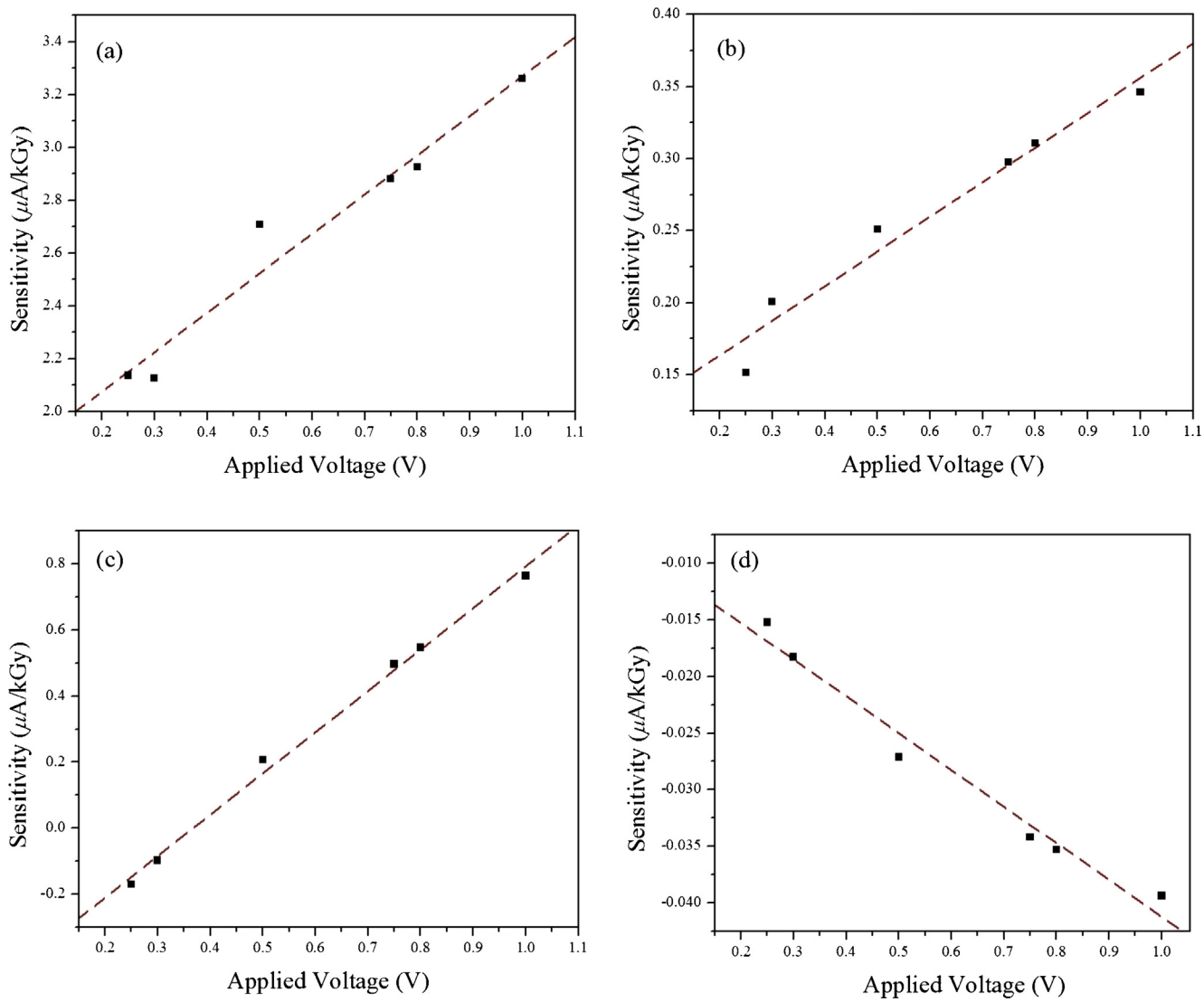

Fig. 13. Effect of radiation dose on output current at bias of (a) 0.25 V, low doses, (b) 1 V, low doses, (c) 0.25 V, high doses, (b) 1 V, high doses. The curves indicate Sensitivity up to 3.259 μA/kGy in case of low radiation doses at 1 V bias voltage.

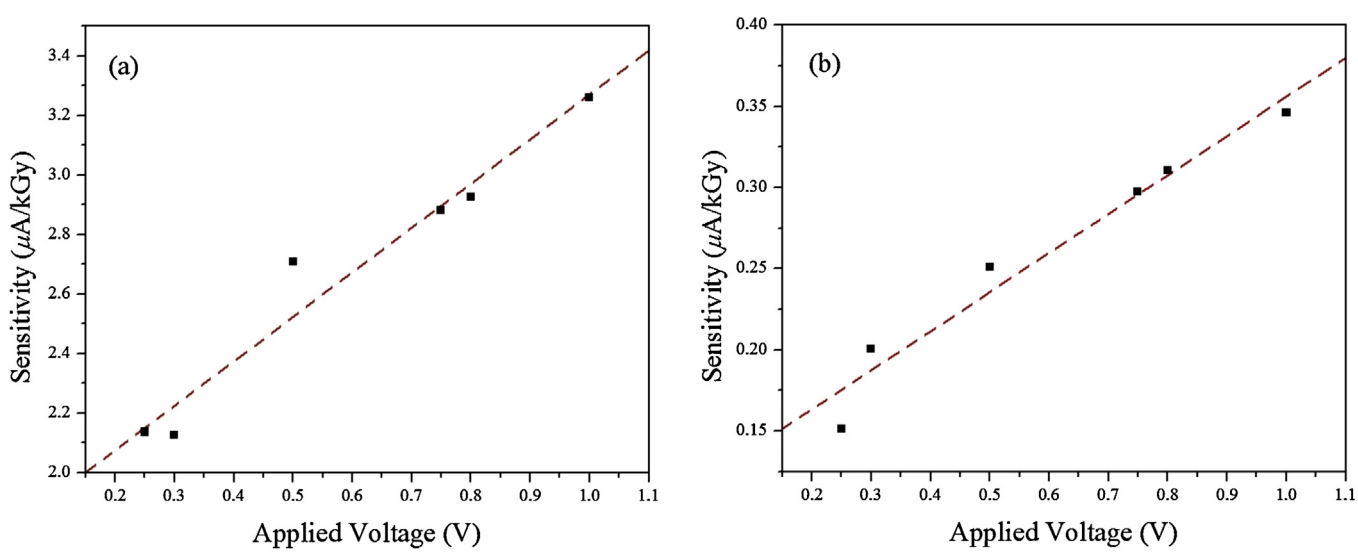

Fig. 14. Device sensitivity at different bias voltages for (a) low radiation doses, (b) high radiation doses.

Fig. 15. Comparison of the sensitivity of graphene–Schottky devices vs. conventional Pt/n-Si devices at different bias voltages of (a) 0.25 V, (b) 0.5 V, (c) 0.75 V, (d) 1 V at a range of radiation doses. Clearly indicating the significant drop in sensitivity of the Pt/n-Si devices at higher radiation doses.

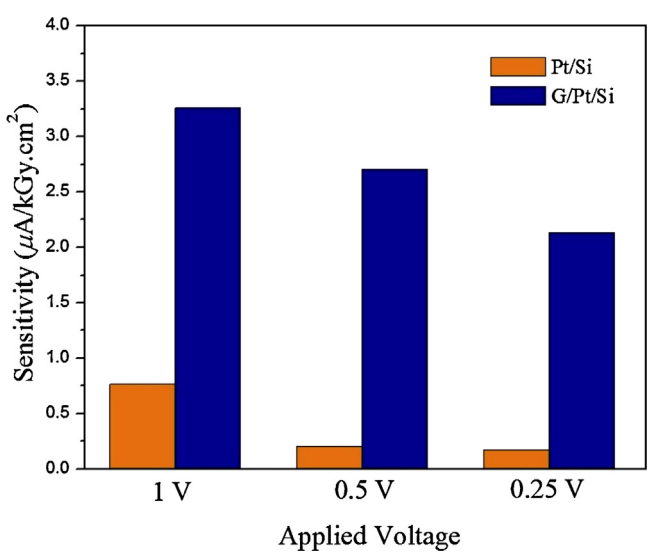

Fig. 16. Comparing the sensitivity of the graphene–Schottky devices vs. Pt/n-Si indicating up to 11 times enhancement of sensitivity at 0.5 V and 0.25 V bias.

increase in sensitivity can be achieved in the graphene–Schottky devices at a bias of 0.25 V as compared to the conventional junction.

3.5. *Effects of repeated irradiation*

Several samples of each device were irradiated and re-irradiated according to the scheme listed in Table 1. Study of the I–V characteristics of the devices revealed acceptable drifts that are estimated at an average of ±0.2422 μA/kGy cm^2 at 0.25 V and low radiation doses which is equivalent to ~10.8% of the device's sensitivity at that specific bias. The average drift is estimated to be ±0.2156 μA/kGy cm^2 at 1 V bias, which is equivalent to ~6.61% of the device's sensitivity at that specific bias. The drift can be attributed to variations in CVD and ALD processes, deposition uniformity across the Si wafer, temperature variations, and Co^{60} source variations.

4. Conclusions

A new device concept has been demonstrated for achieving highly sensitive and wide detection range nanostructured radiation sensors by integrating graphene to a Schottky junction. The key idea is that the current flowing through the Schottky junction

is dominantly controlled by the junction's characteristics (i.e., SBH, and barrier's width), which is very sensitive to the stimuli around the junction, such as γ-photons in our case.The charge transport mechanisms were tested at elevated temperatures yielding results within theoretical models that verified tunneling as the dominant charge transport in the device. Detectors' functionality at low bias voltages with good sensitivity is directly attributable to the verified tunneling. The detector's sensitivity at low bias voltage is a significant advantage over current standards, an advantage that allows the sensor to operate on small batteries or an energy-harvesting source, ideal for low-cost wireless sensor networks.

We have demonstrated an overall enhancement in sensitivity of up to 11 times and detection range of more than five times as compared to conventional Schottky junctions. The proposed sensor operates on low power, isotropic (i.e., independent of the radiation exposure angle), easy to fabricate, can operate wirelessly, and can be seamlessly integrated in wearable detection devices for ultrahigh sensitivity online monitoring of γ-radiations. Finally, a new set of devices based on graphene–MIS (i.e, metal–insulator–semiconductor) and graphene/Pt/high resistivity Si are currently under investigation by the authors and will be the subjects of further reports.

Acknowledgements

This research was supported by an American University in Cairo (AUC) faculty support research grant.

References

[1] National Academy of Engineering, Engineering's Grand Challenges, National Academy of Engineering, 2008.
[2] International Atomic Energy Agency, Nuclear Security Report, 5 September, 2011.
[3] B.K. Sovacool, A critical evaluation of nuclear power and renewable electricity in Asia, J. Contemp. Asia 40 (2010) 379–380.
[4] S. Waguespack, B. Millet, C.G. Wilson, Integrated system for wireless radiation detection and tracking, 2007, IEEE Region 5 Technical Conference (2007) 29–31.
[5] A. Oed, Position-sensitive detector with microstrip anode for electron multiplication with gases, Nuclear instruments and methods in physics research, section A: Accelerators, spectrometers, detectors, and associated equipment, vol. 263, no. 2–3, pp. 351–359, January 1988.
[6] J. Miyamoto, et al., Passivation micro-strip gas chambers with an interstitial germanium coating, IEEE Trans. Nucl. Sci. vol. 44 (no. 3, June) (1997) 660–664.
[7] T. Nakamura, Usage of a capillary plate as a pre-gas-amplification device for neutron microstrip gas chamber, IEEE Trans. Nucl. Sci. vol. 1 (no. 4, August) (2004) 1519–1523.
[8] J.F.C.A. Veloso, J.M.F. Dos Santos, C.A.N. Conde, A proposed new microstructure for gas radiation detectors: microhole and strip plate, Rev. Sci. Instrum. vol. 71 (no. 6, June) (2000) 2317–2376.
[9] S. Park, Y.K. Kim, J.K. Kim, Neutron detection with a GEM, IEEE Trans. Nucl. Sci. vol. 52 (no. 5, October) (2005) 1689–1692.
[10] K. Osberg, et al., A hand-held neutron detector sensor system, IEEE International Symposium on Circuits and Systems (2006).
[11] F.H. Ruddy, et al., The fast neutron response of 4H silicon carbide semiconductor radiation detectors, IEEE Trans. Nucl. Sci. vol. 53 (no. 3, June) (2006) 1666–1670.
[12] S. Metzger, et al., Silicon carbide radiation detector for harsh environments, Proceedings of the European conference on radiation and its effects on components and systems (2002) 51–56.
[13] D.S. McGregor, et al. Design considerations for thin film coated semiconductor thermal neutron detectors – I: Basics regarding alpha particle emitting neutron reactive films, Nuclear instruments and methods in physics research, section A: Accelerators, spectrometers, detectors, and associated equipment, vol. 500, no 1–3, pp. 272–308, November 2003.
[14] D.S. McGregor, et al., Perforated semiconductor neutron detector modules for detection of spontaneous fission neutrons, IEEE Conference on technologies for homeland security: Enhancing critical infrastructure dependability (2007) 162–167.
[15] S. Normand, et al., Study of a new boron loaded plastic scintillator, IEEE Trans. Nucl. Sci. vol. 49 (no. 2, April) (2002) 577–582.
[16] J.S. Neal, et al., A new scintillator for fast neutron detection: single-crystal CeCl3(CH.30H) 4, IEEE Trans. Nucl. Sci. vol. 57 (no. 3, June) (2010) 1692–1696.
[17] M. Katagiri, et al. Scintillation materials for neutron imaging detectors, Nuclear instruments and methods in physics research, section A: Accelerators, spectrometers, detectors, and associated equipment, vol. 529, no. 1–3, pp. 274–279, August 2004.
[18] L. Swiderski, et al., Boron-10 loaded BC523A liquid scintillator for neutron detection in the border monitoring, IEEE Trans. Nucl. Sci. vol. 55 (no. 6) (2008) 3710–3716.
[19] E. Kamaya, et al. Organic scintillators containing 10B for neutron detection,Nuclear instruments and methods in physics research, section A: Accelerators, spectrometers, detectors, and associated equipment, vol. 529, no 1–3, pp. 329–331, August 2004.
[20] M. Petasecca, et al., Thermal and electrical characterization of silicon photomultiplier, IEEE Trans. Nucl. Sci. vol. 55 (no. 3, June) (2008) 1686–1690.
[21] R. Dasaka, S. Pellegrin, M. Kamavaram, C. Wilson, Micromachined scintillation device with charge conversion nanoparticles for neutron and beta particle detection, Proceeding MicroTas (2005) 472–475.
[22] S. Pellegrin, C. Whitney, C.G. Wilson, A multichannel nanoparticle scintillation microdevice with integrated waveguides for alpha, beta, gamma, X-ray, and neutron detection, J. Microelectromech. Syst. vol. 19 (no. 5, October) (2010) 1207–1214.
[23] L. Wang, J. Tang, Q.A. Huang, Gamma and electron beam irradiation effects on the resistance of micromachined polycrystalline silicon beams, Sens. Actuat. A 177 (2012) 99–104.
[24] A. Khusainov, R. Arlt, P. Siffert, Performance of a high resolution CdTe and CdZnTe P-I-N detectors, Nucl. Instrum. Methods Phys. Res. A vol. 380 (no. 1–3, October) (1996) 245–251.
[25] M. Niraula, D. Mochizuki, T. Aoki, Y. Hatanaka, Y. Tomita, T. Nihashi, Improved spectrometric performance of CdTe radiation detectors in a p-i-n design, Appl. Phys. Lett. vol. 75 (no. 15, October) (1999) 2322–2324.
[26] T. Takahashi, S. Watanabe, M. Kouda, G. Sato, Y. Okada, S. Kubo, Y. Kuroda, M. Onishi, R. Ohno, High-resolution CdTe detector andapplications to imaging devices, IEEE Trans. Nucl. Sci. vol. 48 (no. 3, pt. 1, June) (2001) 287–291.
[27] M. Serry, A. Gamal, M. Shaban, A. Sharaf, High sensitivity optochemical and electrochemical metal ion sensor, Micro & Nano Letters 8 (11) (2013) 775–778.
[28] A. Sharaf, A. Gamal, M. Serry, New nanostructured Schottky diode gamma-ray radiation sensor, Procedia Eng. Vol. 87 (2014) 1184–1189.
[29] M. Serry, A. Rubin, M. Ibrahem, S. Sedky, Silicon Germanium as a novel mask for silicon deep reactive ion etching, J. Microelectromechanical Syst. 22 (5) (2013) 1081–1088.
[30] M. Shaban, A.G.A. Hady, M. Serry, A New Sensor for Heavy Metals Detection in Aqueous Media, IEEE Sensors J. vol.14 (2) (2014) 436–441, http://dx.doi.org/10.1109/JSEN.2013.2279916
[31] A.H. Sharaf, A. Gamal, M. Serry, High performance NEMS ultrahigh sensitive radiation sensor based on platinum nanorods capacitor, IEEE SENSORS (3-6 Nov) (2013) 1–4, http://dx.doi.org/10.1109/ICSENS.2013.6688421
[32] L. Wang, H. Dou, Z. Lou, T. Zhang, Encapsuled nanoreactors ($AuSnO_2$): a new sensing material for chemical sensors, Nanoscale 5 (2013) 2686–2691.
[33] A. Lajn, H. v. Wenckstern, Z. Zhang, C. Czekalla, G. Biehne, J. Lenzner, H. Hochmuth, M. Lorenz, M. Grundmann, S. Wickert, C. Vogt, R. Denecke, Properties of reactively sputtered Ag, Au, Pd, and Pt Schottky contacts on *n*-type ZnO, J. Vac. Sci. Technol. B 27 (2009) 1769–1773.
[34] I.T. Weber, A. Valentini, L.F.D. Probst, E. Longo, E.R. Leite, Influence of noble metals on the structural and catalytic properties of Ce-doped SnO2 systems, Sens. Actuat. B 97 (2004) 31–38.
[35] L. Wang, Z. Lou, R. Wang, T. Fei, T. Zhang, Ring-like PdO–NiO with lamel- lar structure for gas sensor application, J. Mater. Chem. 22 (2012) 12453–12456.
[36] M. Lopez-Garcia, Y.-L.D. Ho, M.P.C. Taverne, L.-F. Chen, M.M. Murshidy, A.P. Edwards, M.Y. Serry, A.M. Adawi, J.G. Rarity, R. Oulton, Efficient out-coupling and beaming of Tamm optical states via surface plasmon polariton excitation, Applied Physics Letters 104 (no. 23) (2014) 231116.
[37] G. Ramírez, S.E. Rodil, S. Muhl, D. Turcio-Ortega, J.J. Olaya, M. Rivera, E. Camps, L. Escobar-Alarcón, Amorphous niobium oxide thin films, J. Non-Cryst. Solids 356 (2010) 2714–2721.
[38] M.K. Siddiki, S. Venkatesan, Q. Qiao, Nb2O5 as a new electron transport layer for double junction polymer solar cells, Phys. Chem. Chem. Phys. 14 (2012) 4682–4686.
[39] X. Fang, L. Hu, K. Huo, B. Gao, L. Zhao, M. Liao, P.K. Chu, Y. Bando, D. Golberg, New ultraviolet photodetector based on individual Nb2O5 nanobelts, Adv. Funct. Mater. 21 (2011) 3907–3915.
[40] J.Z. Ou, R.A. Rani, M.-H. Ham, M.R. Field, Y. Zhang, H. Zheng, P. Reece, S. Zhuiykov, S. Sriram, M. Bhaskaran, R.B. Kaner, K. Kalantar-zadeh, Elevated temperature anodized Nb2 O5: a photoanode material with exceptionally large photocon- version efficiencies, ACS Nano 6 (2012) 4045–4053.
[41] A. Reina, X. Jia, J. Ho, D. Nezich, H. Son, V. Bulovic, M.S. Dresselhaus, J. Kong, Nano Lett. 9 (2009) 30.
[42] K.S. Kim, Y. Zhao, H. Jang, S.Y. Lee, J.M. Kim, K.S. Kim, J. Ahn, J. Kim, B.H. Hong, Nature 457 (2009) 706.
[43] X.S. Li, W.W. Cai, J.H. An, S. Kim, J. Nah, D.X. Yang, A. Piner, I. Velamakanni, E. Jung, L. Banerjee, R.S. Ruoff, Science 324 (2009) 1312.
[44] X. Li, G. Zhang, X. Bai, X. Sun, X. Wang, E. Wang, H. Dai, Nat. Nanotechnol. 3 (2008) 538.
[45] Y. Hernandez, V. Nicolosi, M. Lotya, F.M. Blighe, Z. Sun, S. De, I.T. McGovern, B. Holland, M. Byrne, Y.K. Gun'Ko, J.J. Boland, P. Niraj, G. Duesberg, S. Krishnamurthy, R. Goodhue, J. Hutchinson, V. Scardaci, A.C. Ferrari, J.N. Coleman, Nat. Nanotechnol. 3 (2008) 563.

[46] J.F. Tressler, S. Alkoy, R.E. Newnham, Piezoelectric sensors and sensor materials, J. Electroceram. 4 (1998) 257–272.
[47] L.M. Rodriguez, D.R. Gallagher, M.W. Gallagher, B.H. Fisher, J.R. Humphries, D.C. Malocha, Wireless SAW sensor temperature extraction precision, IEEE Sens. J. 14 (2014) 3830–3837.
[48] W. Bulst, G. Fischerauer, L. Reindl, State of the art in wireless sensing with surface acoustic waves, IEEE Trans. Ind. Electron. 2 (2001) 265–271.
[49] S.M. Sze, K.K. Ng, Physics of Semiconductor Device, John Wiley & Sons, Inc. Publication, 2006.
[50] C.R. Crowell, S.M. Sze, Current transport in metal-semiconductor barriers, Solid-State Electron. 9 (1966) 1035–1048.
[51] V. Yu, E. Whiteway, J. Maassen, M. Hilke, Phys Rev. B 84 (2011) 205407.
[52] L.S. Yu, et al., The Origins of Leaky Characteristics of Schottky Diodes on p-GaN, IEEE Trans. Electron Devices 50 (2003) 292–296.
[53] L.S. Yu, Q.Z. Liu, D.J. Qiao, S.S. Lau, J.M. Redwing, The role of the tunneling component in the current–voltage characteristics of metal–GaN Schottky diodes, J. Appl. Phys. vol. 84 (1998) 2099–2104.
[54] B. Van Zeghbroeck, Principles of Semiconductor Devices, Prentice Hall, 2011.